J. Fluid Mech. (1998), *vol.* 377, *pp.* 347–373. Printed in the United Kingdom

The structure of wall-pressure fluctuations in turbulent boundary layers with adverse pressure gradient and separation

By Y. NA AND P. MOIN†

Department of Mechanical Engineering, Stanford University, Stanford, CA 94305, USA

(Received 25 July 1997 and in revised form 31 March 1998)

Space–time correlations and frequency spectra of wall-pressure fluctuations, obtained from direct numerical simulation, are examined to reveal the effects of pressure gradient and separation on the characteristics of wall-pressure fluctuations. In the attached boundary layer subjected to adverse pressure gradient, contours of constant two-point spatial correlation of wall-pressure fluctuations are more elongated in the spanwise direction. Convection velocities of wall-pressure fluctuations as a function of spatial and temporal separations are reduced by the adverse pressure gradient. In the separated turbulent boundary layer, wall-pressure fluctuations are reduced inside the separation bubble, and enhanced downstream of the reattachment region where maximum Reynolds stresses occur. Inside the separation bubble, the frequency spectra of wall-pressure fluctuations normalized by the local maximum Reynolds shear stress correlate well compared to those normalized by free-stream dynamic pressure, indicating that local Reynolds shear stress has more direct influence on the wall-pressure spectra. Contour plots of two-point correlation of wall-pressure fluctuations are highly elongated in the spanwise direction inside the separation bubble, implying the presence of large two-dimensional roller-type structures. The convection velocity determined from the space–time correlation of wall-pressure fluctuations is as low as $0.33U_0$ (U_0 is the maximum inlet velocity) in the separated zone, and increases downstream of reattachment.

1. Introduction

Wall-pressure fluctuations in turbulent boundary layers are of direct importance in many engineering applications involving flow-induced vibration, aircraft cabin noise and hydroacoustics of under-water vehicles. Structural models of flow-induced vibration or sound require frequency/wavenumber spectra of wall-pressure fluctuations as a forcing function input. Blake (1986) has reviewed this subject extensively. Many investigations of the fluctuating wall-pressure field beneath a turbulent boundary layer, aimed at enhancing our understanding of the structure of turbulence or providing data needed in engineering applications, have been performed in the past 40 years. The first measurement of wall-pressure fluctuations in a zero-pressure-gradient (ZPG) turbulent boundary layer was reported by Willmarth (1956). He found that the ratio of r.m.s. wall-pressure to dynamic pressure was approximately 0.0035. Most of the theoretical and experimental studies that followed Willmarth's work have been performed in ZPG turbulent boundary layers (e.g. Bull 1967; Blake 1970; Farabee

† Also with NASA Ames Research Center.

& Casarella 1991). Turbulent boundary layers with non-zero pressure gradients have been explored in less depth. Accurate measurements are made difficult by the sensitivity to the measuring probe or the pressure transducer size, and the wide range of scales of the pressure fluctuations. Willmarth (1975) provided a comprehensive review of the experimental findings on the wall-pressure fluctuations and Eckelmann (1989) has published an updated review.

For equilibrium turbulent boundary layers with adverse pressure gradient (APG), the low-frequency part of the spectrum scales approximately on the local maximum shear stress in the boundary layer (Mabey 1982; Simpson, Ghodbane & McGrath 1987). Mabey (1972) summarized some measurements of pressure fluctuations and presented spectra for step-induced separation and reattaching flows. He found that the pressure fluctuations, $p_{r.m.s.}$, at the reattachment point normalized by local dynamic pressure, q_∞, were approximately 0.06 and 0.1 for the backward-facing step flow and forward-facing step flow, respectively. Kiya, Sasaki & Arie (1982) showed similar results for a forward-facing step flow; their $p_{r.m.s.}/q_\infty$ reached a maximum of 0.14 at the reattachment point.

Simpson *et al.* (1987) studied the effects of APG on the wall-pressure fluctuations in a separated turbulent boundary layer over a flat plate. Much higher levels of noise and pressure fluctuations are produced by a separated flow as compared to an attached boundary layer. Since the Reynolds stresses and their gradients are large away from the wall, it has been speculated that the largest pressure fluctuations are not at the wall, but away from the wall. The r.m.s. of wall-pressure fluctuations, $p_{r.m.s.}$, increases monotonically through the APG attached flow region and detached flow zone. Spectra of wall-pressure fluctuations, $\phi(\omega)$, for $\omega\delta^*/U_\infty > 0.001$ are correlated well when normalized by the maximum shearing stress, $-\rho\overline{u'v'}_{max}$. For the attached flow $\phi(\omega) \sim \omega^{-0.7}$ at low frequencies while $\phi(\omega) \sim \omega^{-3}$ at higher frequencies in the strong APG region. After the beginning of intermittent backflow, $\phi(\omega) \sim \omega$ at low frequencies and ω^{-3} at high frequencies. Farther downstream the lower-frequency range varies as $\omega^{1.4}$.

Recently, direct numerical simulation (DNS) databases have become available for the study of wall-pressure fluctuations. Handler *et al.* (1984) obtained the wall-pressure field in a channel flow from a coarse grid DNS. Their spectrum differed from the experimental measurements at high frequencies which was attributed to the difference in Reynolds number and limited spatial resolution.

Kim (1989) and Choi & Moin (1990) used the database of Kim, Moin & Moser (1987) to study the structure of pressure fluctuations in a turbulent channel flow. Choi & Moin computed the frequency/wavenumber spectra and convection velocity of wall-pressure fluctuations and found that small-scale motions had a smaller convection velocity of $0.6U_0$ to $0.7U_0$ (U_0 is the centreline velocity) and large-scale structures, corresponding to large separations in space or time, had a convection velocity of about $0.8U_0$.

Neves & Moin (1994) studied the effects of convex transverse curvature on wall-pressure fluctuations through direct numerical simulations of axial flow boundary layers on long cylinders. As the curvature increases, the r.m.s. pressure fluctuations decrease. However, the effect of curvature is small on the fractional contributions from various layers (inner and outer) in the flow to the wall-pressure fluctuations.

The databases used in the present study were obtained from direct numerical simulations of two spatially evolving turbulent boundary layers over a flat plate with different pressure gradients, created by prescribed vertical velocity distributions along

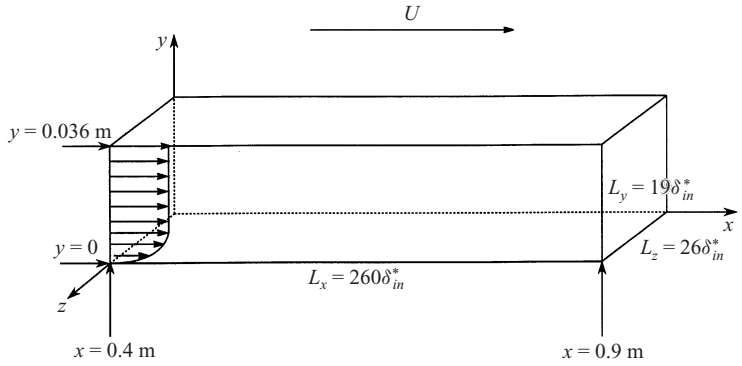

FIGURE 1. Computational domain for the adverse pressure gradient flow.

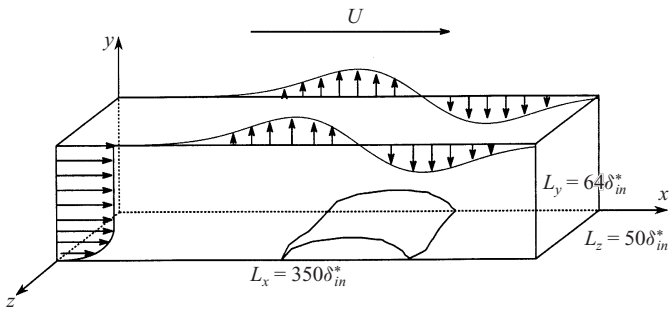

FIGURE 2. Computational domain of the separated turbulent boundary layer.

the upper boundary of the computational domain. In the first boundary layer, the adverse pressure gradient is relatively mild and the boundary layer remains attached to the wall. The wall-pressure distribution and the Reynolds number were matched to those of Watmuff's (1989) experiment, as were the gross characteristics of the boundary layer at the inlet. In the second case, a suction–blowing velocity profile along the top boundary created a strong adverse-to-favourable pressure gradient, and a separated boundary layer resulted. These flows will be described in detail in § 3 and § 4, respectively.

2. Numerical method

The numerical method and boundary conditions used to generate the DNS database investigated in the present study are documented in detail in Na & Moin (1996, 1998). Only a brief summary is given below.

The three-dimensional computational domains used for the present study are shown in figures 1 and 2. The streamwise extent of the domain is L_x, the vertical height is L_y and the spanwise extent is L_z. All dimensions are normalized by the inlet displacement thickness, δ^*_{in}. To facilitate comparisons with Watmuff's (1989) experiment, the dimensional length units (in metres) are also noted in figure 1.

The non-dimensional incompressible Navier–Stokes and continuity equations with constant density and kinematic viscosity are

$$\frac{\partial}{\partial t}u_i + \frac{\partial}{\partial x_k}u_i u_k = -\frac{\partial}{\partial x_i}p + \frac{1}{Re_{\delta^*_{in}}}\frac{\partial^2}{\partial x_k \partial x_k}u_i, \tag{2.1}$$

$$\frac{\partial}{\partial x_k}u_k = 0. \tag{2.2}$$

All variables are non-dimensionalized by the maximum mean velocity at inlet, U_0, and the inlet displacement thickness, δ^*_{in}. The subscripts i, j, k take values of 1, 2, 3 to denote the streamwise (x), wall-normal (y) and spanwise (z) directions, respectively. The u_i are the velocity components and p is the static pressure. The Reynolds number, $Re_{\delta^*_{in}}$, is defined by the displacement thickness at the inlet, δ^*_{in}, and maximum mean inlet velocity, U_0. The governing equations (1) and (2) were solved using a semi-implicit scheme with the modified fractional step procedure (Le & Moin 1991). It employs a second-order central difference for spatial discretization and a staggered mesh with uniform spacing in x and z and variable spacing in y. The time advancement is of third-order Runge–Kutta type in conjunction with Crank–Nicolson treatment for the viscous terms. The Poisson equation for pressure is solved only at the final Runge–Kutta substep by a Fourier transform method.

The no-slip boundary condition is used along the lower boundary of the computational domain. Since the flow is assumed to be homogeneous in the spanwise direction, periodic boundary conditions are used in that direction. At the exit of the computational domain, the convective boundary condition was used (Pauley, Moin & Reynolds 1990). A vertical velocity distribution, $V_{top}(x)$, is specified at the top boundary to generate the desired pressure gradient in the boundary layers. In addition, the vorticity is set to zero at the top boundary. The inflow boundary conditions are provided by a sequential feeding of a frozen DNS field generated from a temporal simulation based on Taylor's hypothesis. To minimize the periodicity effects arising from recycling the same flow field, its amplitude factors in Fourier (wavenumber) space were randomized (Mahesh, Moin & Lele 1996). The phase angles are kept unchanged to preserve the turbulence structure. Spalart's (1988) temporal simulation data of ZPG turbulent boundary layer at Reynolds numbers of 300 and 670 based on momentum thickness were used to generate the velocity fluctuations for the separated turbulent boundary layer and the attached boundary layer with APG, respectively. DNS of ZPG turbulent boundary layers with this inflow turbulence (Na & Moin 1996) shows that the flow recovers very quickly after a short transition length: evolution of skin friction coefficient, C_f, indicates that the recovery distance is less than about $20\delta^*_{in}$.

In the simulation of the attached boundary layer with pressure gradients, we specified a blowing–suction velocity distribution $V_{top}(x)$ (figure 3 *a*) along the upper boundary so that the computed wall-pressure coefficient (C_p) distribution matches that of Watmuff's (1989) experiment. This method differs from the so-called 'inverse calculation method' where the pressure gradient or the velocity at the edge of boundary layer is determined as part of the solution by specification of a displacement thickness or wall-shear stress distribution. Since there is no systematic way of achieving this boundary condition in a turbulent boundary layer, an iterative procedure was used. Starting with an initial guess for $V_{top}(x)$, the governing equations are solved and the computed C_p distribution is compared with that of the experiment. If the

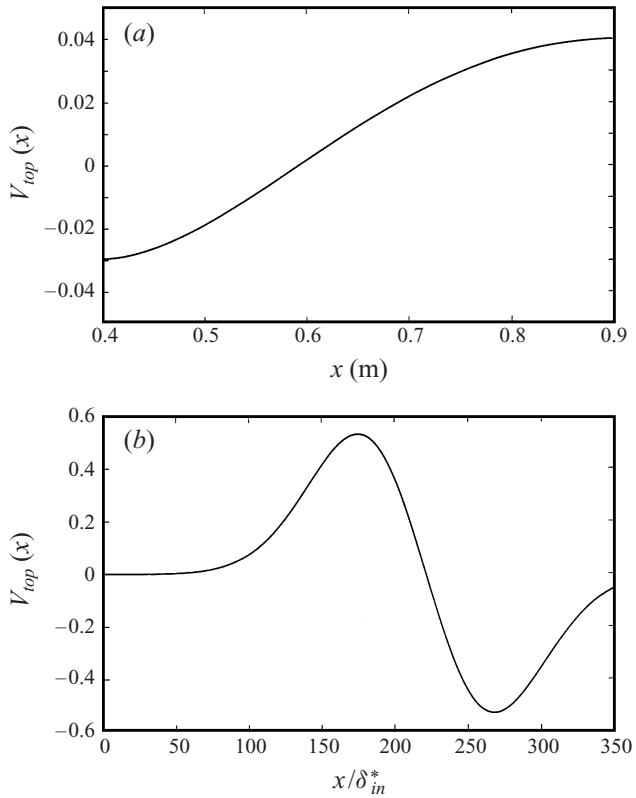

FIGURE 3. Suction–blowing velocity distributions along the upper boundary: (*a*) attached boundary layer; (*b*) separated turbulent boundary layer.

agreement is not good, corrections are made to $V_{top}(x)$ and calculations are repeated until the agreement is satisfactory. Since the velocities at the edge of the boundary layer are known from the experimental data, the potential flow solution which gives the same velocity distribution along the edge of the boundary layer can be used as an initial guess. The potential flow solution was obtained by the panel method in the present work.

In the simulation of the separated turbulent boundary layer, a suction–blowing velocity profile, $V_{top}(x)$, was prescribed along the upper boundary of the computational domain. Figure 3(*b*) shows the suction–blowing distribution which leads to the APG needed to produce a separation bubble. The strong favourable pressure gradient (FPG) induced by the blowing velocity distribution of $V_{top}(x)$ causes the layer to firmly reattach after the flow separates. The maximum $V_{top}(x)$ was adjusted so that the height of the separation bubble is about two inlet boundary layer thicknesses.

The power spectra and space–time correlations of wall-pressure fluctuations were calculated using the standard techniques for stochastic time signals. Pressure fields were saved at equally spaced points in the time interval $0 \leqslant t \leqslant T_N$ (where T_N is the total integration time). The record was divided into m overlapping intervals (with 50% overlap). Since the data are not periodic in any of the intervals, at the edges of the intervals the data were tapered by a Hanning 'window function'. All spectra presented in this paper were obtained using an ensemble average over the m realizations. For details, see Choi & Moin (1990).

3. Attached turbulent boundary layer with pressure gradients

3.1. *Flow configuration and computational resolution*

The computational domain is shown in figure 1. The Reynolds number based on the momentum thickness and maximum mean streamwise velocity at the inlet is 670.

The APG starts from $x = 0.6$ m and is preceded by a FPG region from $x = 0.4$ m. This is to help the flow lose its memory of the initial transients due to artificial inflow turbulence. The simulation without adding the FPG region showed significant discrepancies between the computed and experimental results in the APG region. This is expected because APG flows are very sensitive to the upstream conditions. Inman & Bradshaw (1981) estimated that 20 boundary layer thicknesses are sufficient for turbulence to develop well as indicated by a logarithmic layer. In the present study, the extent of the FPG region is about 15 times the inlet boundary layer thickness.

The upper boundary should be located far enough away from the wall to allow the vortical structures inside the boundary layer to grow without being affected by blockage effects, and to guarantee the no-vorticity condition in the free stream. The extent of the domain in the wall-normal direction was chosen to be 0.036 m or about 1.4 times the boundary layer thickness at $x = 0.89$ m, the exit plane of the computational domain. The computed results with this computational box show that the upper boundary is located in the region of negligible vorticity.

The period in z, L_z, is 0.048 m or about 1.8 times the maximum boundary layer thickness at the exit plane. The two-point velocity correlations indicate that the mean width of the largest structures at $x = 0.89$ m is about 0.014 m indicating that the computational domain size chosen in the spanwise direction is adequate. The computation was conducted with $768 \times 65 \times 258$ grid points in the x-, y- and z-directions. The grid spacing in wall units, ν/u_τ, based on inlet parameters was $\Delta x^+ = 16.6$ and $\Delta z^+ = 4.8$. In the wall-normal direction, $\Delta y^+_{min} = 0.56$ at the wall and $\Delta y^+_{max} = 35.5$ in the free stream. Extensive grid-dependence studies were conducted to ensure adequacy of the grid spacing chosen. These studies showed that flow characteristics are more influenced by the spanwise grid spacing than those in the streamwise and wall-normal directions and the C_p distribution (which is essentially an inviscid quantity) is very insensitive to the spatial resolution. Two-point correlations of wall-pressure fluctuations (shown in figure 8) indicate that the domain size in the spanwise direction is adequate for the study of the wall-pressure field.

Governing equations (1) and (2) were integrated in time for 35 200 time steps and the wall-pressure field was stored every 10 time steps (calculation time step Δt_{cal} is 0.02 δ^*_{in}/U_0). 3520 samples were divided into $m = 21$ overlapping segments. Each segment contains 320 samples and covers, $T_N = 64\delta^*_{in}/U_0$. The resulting resolved frequency range is $0 \leqslant \omega \leqslant 15.6U_0/\delta^*_{in}$, with a frequency resolution of $\Delta\omega = 0.098U_0/\delta^*_{in}$. Pointwise quantities were also sampled every 10 calculation time steps and averaged over spanwise direction and time, $T_{ave} = 704\delta^*_{in}/U_0$.

3.2. *Flow fields*

The wall-pressure coefficients C_p of the simulation and of the experiment are compared in figure 4. The overall agreement is very good. As described in § 2, we had to iterate to match the given C_p distribution. Two other non-dimensional pressure gradient parameters are

$$\beta = \frac{\delta^*}{\tau_w}\frac{\mathrm{d}P}{\mathrm{d}x} \quad \text{and} \quad K = \frac{\nu}{U_\infty^2}\frac{\mathrm{d}U_\infty}{\mathrm{d}x};$$

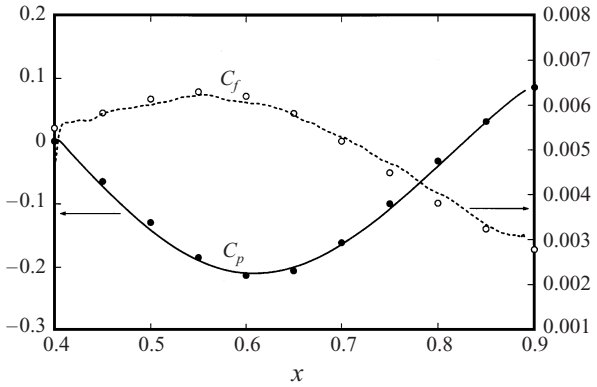

FIGURE 4. Mean wall-pressure and skin friction coefficients based on U_0: ——, – – –, present; •, ○, Watmuff's experiment.

at $x = 0.5$ m, they take the values $\beta \approx -0.35$ and $K \approx 0.93 \times 10^{-6}$. At $x = 0.85$ m, $\beta \approx 1.78$ and $K \approx -0.14 \times 10^{-5}$. The flow is not self-similar in that the pressure gradient parameter β varies with x.

The computed skin friction coefficient C_f, based on U_0, shown in figure 4 is definitely low at $x = 0.4$ m due to the inflow boundary condition. Since the streamwise location $x = 0.4$ m is in the FPG region, C_f at this point is expected to be higher than that in the ZPG turbulent boundary layer at the same Reynolds number. As described in § 2, Spalart's ZPG turbulent boundary layer data for $Re_\theta = 670$ were prescribed at the inflow plane of the computational box and this explains the observed sizeable difference in C_f at $x = 0.4$ m. The skin friction then recovers very quickly by $x = 0.42$ m. After this point the maximum disagreement of 2.2×10^{-4}, which is about 5.8 %, occurs at $x = 0.8$ m.

Turbulence intensities are given in figure 5. At $x = 0.5$ m the agreement is not good since the flow is still in the process of developing from the artificial inflow turbulence, but the subsequent recovery is aided by the FPG. In the APG region, both DNS and experimental profiles continuously change in shape from that of a ZPG turbulent boundary layer to the typical APG boundary layer shape which involves a large fraction of turbulent energy in the outer layer. In the experiment, $u_{r.m.s.}$ was measured by a normal hot wire instead of an X-wire so $u_{r.m.s.}$ is more accurate than $v_{r.m.s.}$ and $w_{r.m.s.}$. The agreement with the experimental data is also better for $u_{r.m.s.}$, and the computed $v_{r.m.s.}$ and $w_{r.m.s.}$ are consistently higher than in the experiment. Similar behaviour can also be seen in Spalart & Watmuff (1993).

The Reynolds shear stress profiles show the same behaviour as in turbulence intensities in that the agreement is improved as one moves downstream (Na & Moin 1996). The DNS results, however, are consistently higher than experimental results. Spalart & Watmuff (1993) inferred that the Reynolds shear stress measurements are underestimated and the true experimental shear stress may be higher than those given in Watmuff (1989).

3.3. *Pressure fluctuations*

In figure 6, the profiles of pressure fluctuations at various streamwise stations are shown. The maxima of pressure fluctuations occur away from the wall. Non-negligible pressure fluctuations outside the boundary layer are due to irrotational fluctuations in the free-stream as discussed by Bradshaw (1967). The pressure fluctuations away

https://doi.org/10.1017/S0022112098003218 Published online by Cambridge University Press

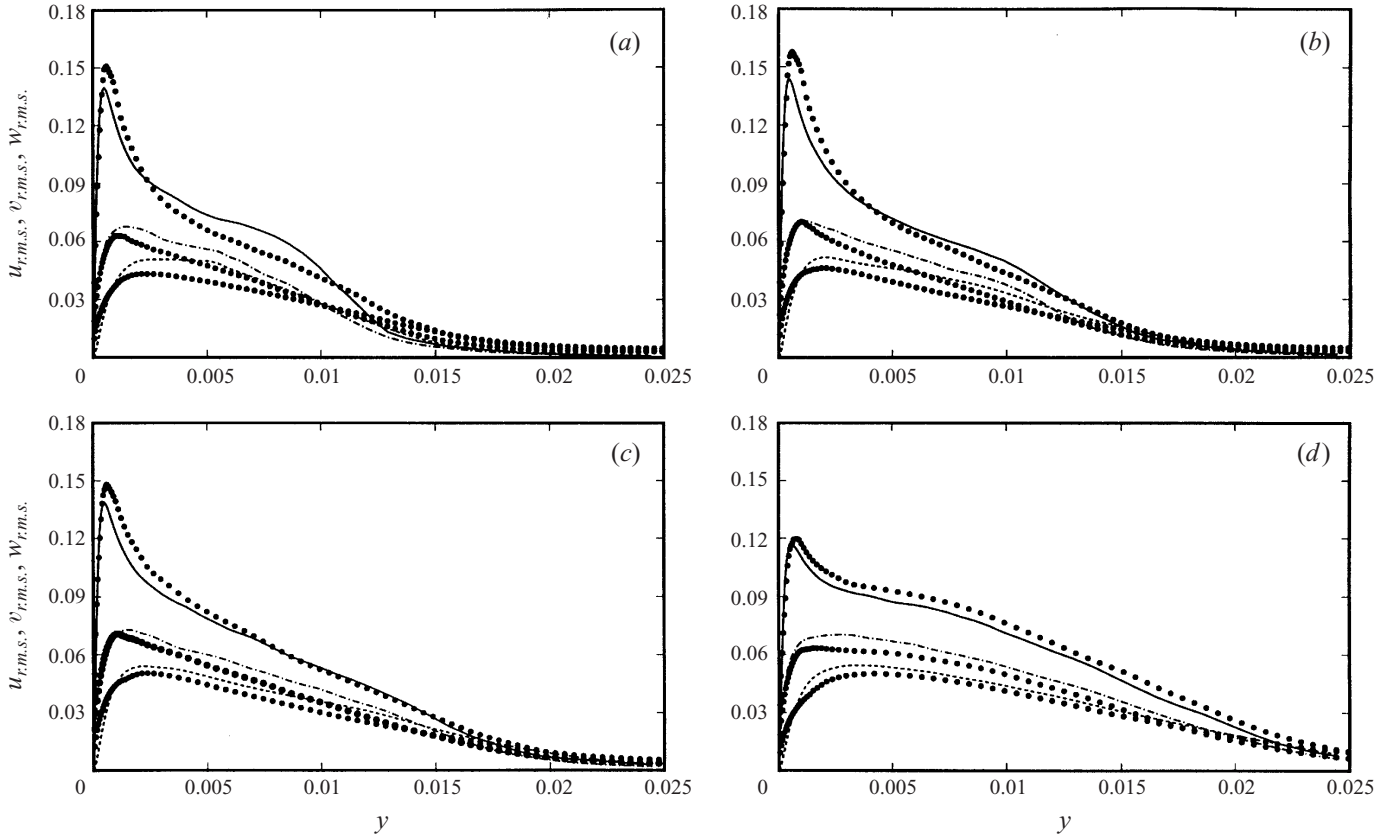

FIGURE 5. Root-mean-square profiles normalized by U_0. •, Watmuff; ——, $u_{r.m.s.}$; – – –, $v_{r.m.s.}$; — · —, $w_{r.m.s.}$. (*a*) $x = 0.5$; (*b*) $x = 0.6$; (*c*) $x = 0.7$; (*d*) $x = 0.85$.

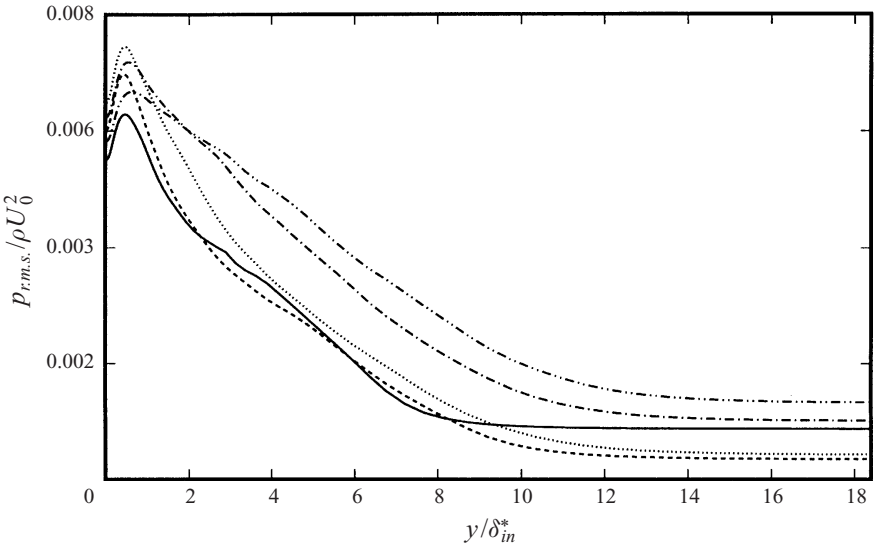

FIGURE 6. Distribution of pressure fluctuations. ——, $x = 0.5$; – – –, $x = 0.6$; · · · · ·, $x = 0.7$; — · —, $x = 0.8$; — · · —, $x = 0.85$.

from the wall ($y/\delta^*_{in} \geqslant 2$) increase with x (in the adverse pressure gradient region which starts at $x \approx 0.6$). The r.m.s. wall-pressure fluctuations normalized by wall shear stress, $p_{r.m.s.}/\tau_w$, vary from 1.85 in the FPG region to 3.7 in the APG region, whereas the wall-pressure fluctuations normalized by maximum Reynolds shear stress, $p_{r.m.s.}/(-\rho\overline{u'v'})_{max}$, take the values of 1.3 in the FPG region and 2.3 in the APG region, indicating that $p_{r.m.s.}/(-\rho\overline{u'v'})_{max}$ has slightly less variation than $p_{r.m.s.}/\tau_w$ as shown by Simpson *et al.* (1987).

Power spectra normalized by local dynamic pressure, q_∞, are shown in figure 7(*a*). Data appear to collapse at low frequencies. For $0.1 < \omega\delta^*/U_\infty < 1$, $\phi(\omega)$ decreases as $\omega\delta^*/U_\infty$ decreases with a slope of about 0.4. Due to the low Reynolds number considered in the present study, there is only a negligible region with -1 slope which arises from the contribution of motions in the logarithmic region. The spectra exhibit small regions with -3 and then -5 slopes in the high-frequency range. With increasing streamwise pressure gradient, power increases in the high-frequency region. Scaling of pressure spectra with τ_w^2 which gives good collapse of data at low frequencies in the ZPG turbulent boundary layer (Na & Moin 1996) and channel flow (Choi & Moin 1990) is not appropriate in the presence of streamwise pressure gradient as indicated in figure 7(*b*). The effect of the Reynolds number on pressure fluctuations can be established from some of the previous works in the literature. In his study of the pressure field in a channel, Kim (1989) stipulated that essential characteristics of the pressure field at low Reynolds numbers would differ only slightly from those of higher Reynolds number flows, except for some features observable only for high Reynolds number flows, such as the inertial subrange in the power spectra of the pressure fluctuations. Also, the effect of Reynolds number on the power spectra can be seen in Choi & Moin (1990). With increasing Reynolds number, power increases in the high-frequency region with outer scaling and power increases in the low-frequency region with inner scaling.

In figure 7(*c*), inner scaling is used for both spectra and frequency. Unlike in the ZPG turbulent boundary layer and channel flow, the spectra do not collapse at high

https://doi.org/10.1017/S0022112098003218 Published online by Cambridge University Press

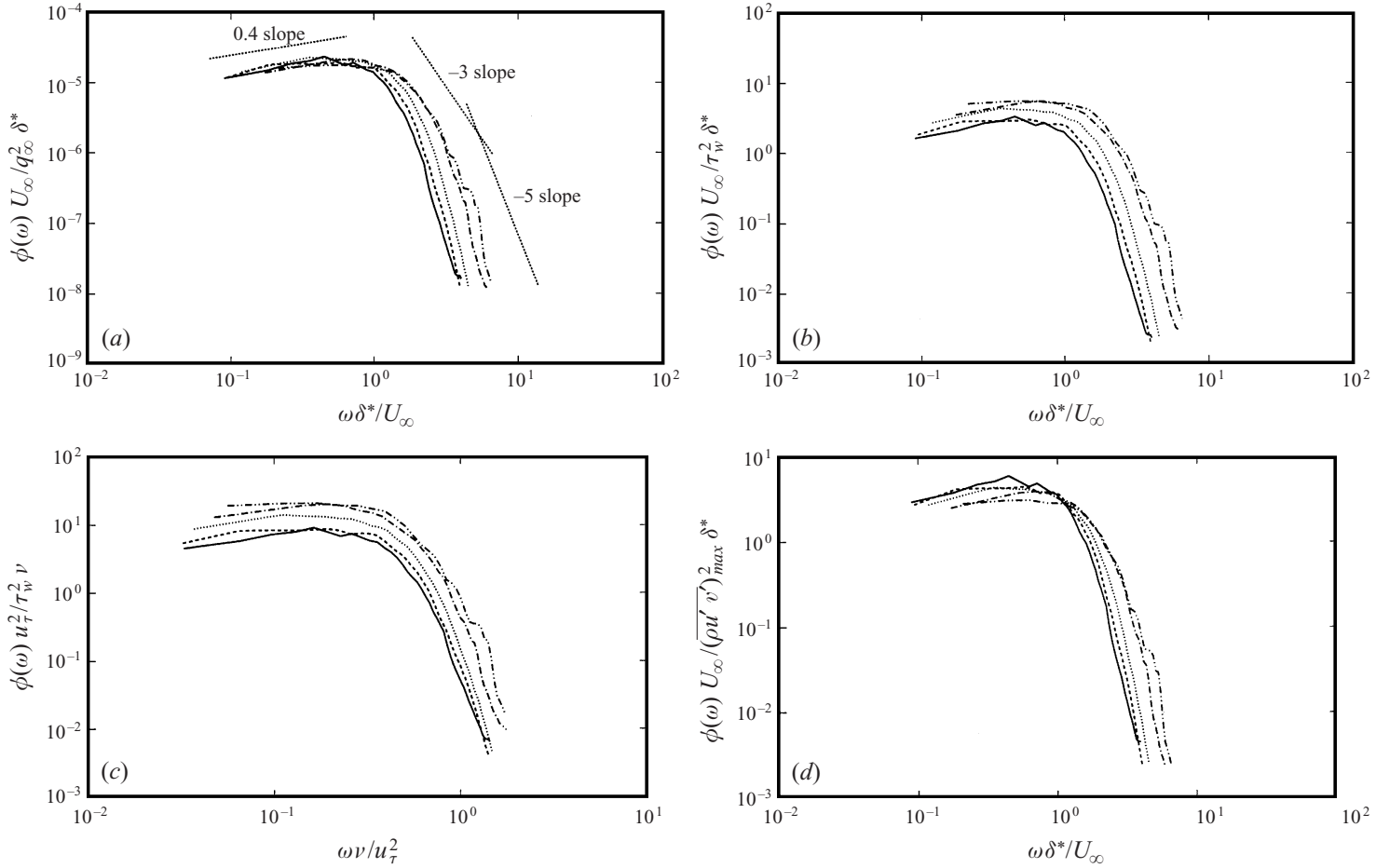

FIGURE 7. Frequency spectra of wall-pressure fluctuations: (*a*) outer variable scaling with pressure scaled with q_∞^2; (*b*) outer variable scaling with pressure scaled with τ_w^2; (*c*) inner variable scaling; (*d*) outer variable scaling with pressure scaled with $(\overline{\rho u' v'})^2_{max}$. ——, $x = 0.5$; – – –, $x = 0.6$; · · · · ·, $x = 0.7$; — · —, $x = 0.8$; — · ·—, $x = 0.85$.

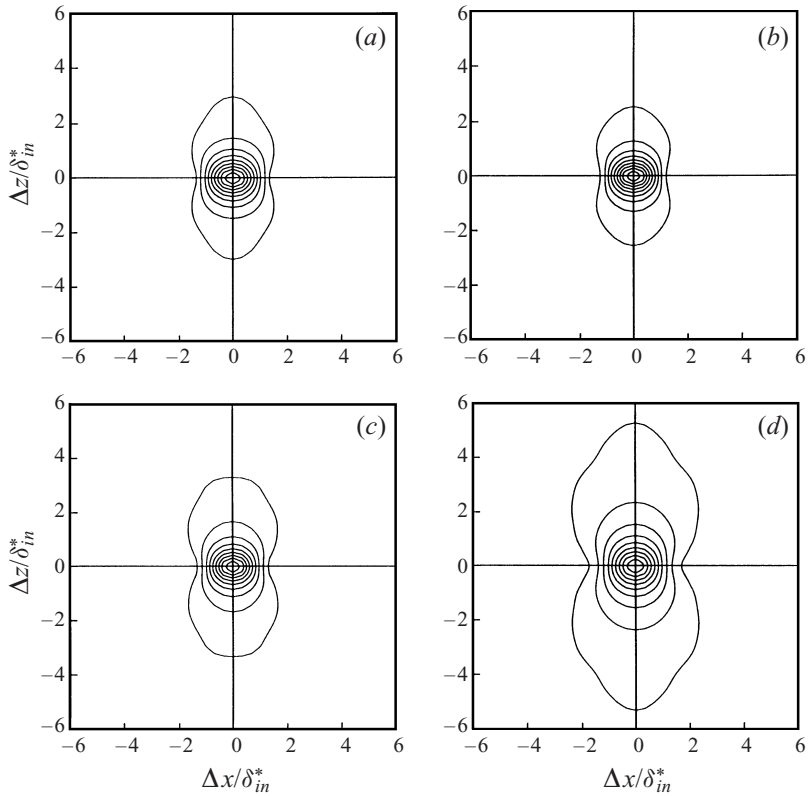

FIGURE 8. Contour plot of two-point correlation of wall-pressure fluctuations as a function of streamwise and spanwise separations. (*a*) $x = 0.5$; (*b*) $x = 0.6$; (*c*) $x = 0.7$; (*d*) $x = 0.85$. Contour levels are from 0.1 to 0.9 with increments of 0.1.

frequencies. Thus, based on figures 7(*b*) and 7(*c*), any scaling with τ_w (or u_τ) does not produce collapsed spectra in the presence of non-negligible pressure gradient. The reason for this is partly due to the fact that the wall shear is not an important parameter in the APG boundary layer, and that the present turbulent boundary layer is not self-similar in that the pressure gradient parameter β is not constant. In figure 7 (*d*), the local maximum Reynolds shear stress is used to scale the pressure. Compared to figure 7 (*a*), the spectra show more variation in the low-frequency range, which may indicate that local dynamic pressure is a better scaling for the similarity in the low-frequency region. This scaling will be further investigated for the case of the separated turbulent boundary layer.

Two-point correlations as a function of streamwise and spanwise spatial separations are shown in figure 8. For the purpose of comparison, the spatial separations are normalized by the inlet displacement thickness. At all streamwise locations, contours at small separations are circular (or nearly isotropic) but at larger separations they are elongated in the spanwise direction. In the FPG region, the spanwise extent of the largest contours (corresponding to contour level 0.1) decreases up to $x = 0.6$ m, and then increases in the APG region. This indicates that the 'pressure' integral length scale in the boundary layer decreases in FPG and increases in APG. In the APG region, the extent of the 0.1 level contour (which is indicative of the large structures) grows faster in the spanwise direction than in the streamwise direction.

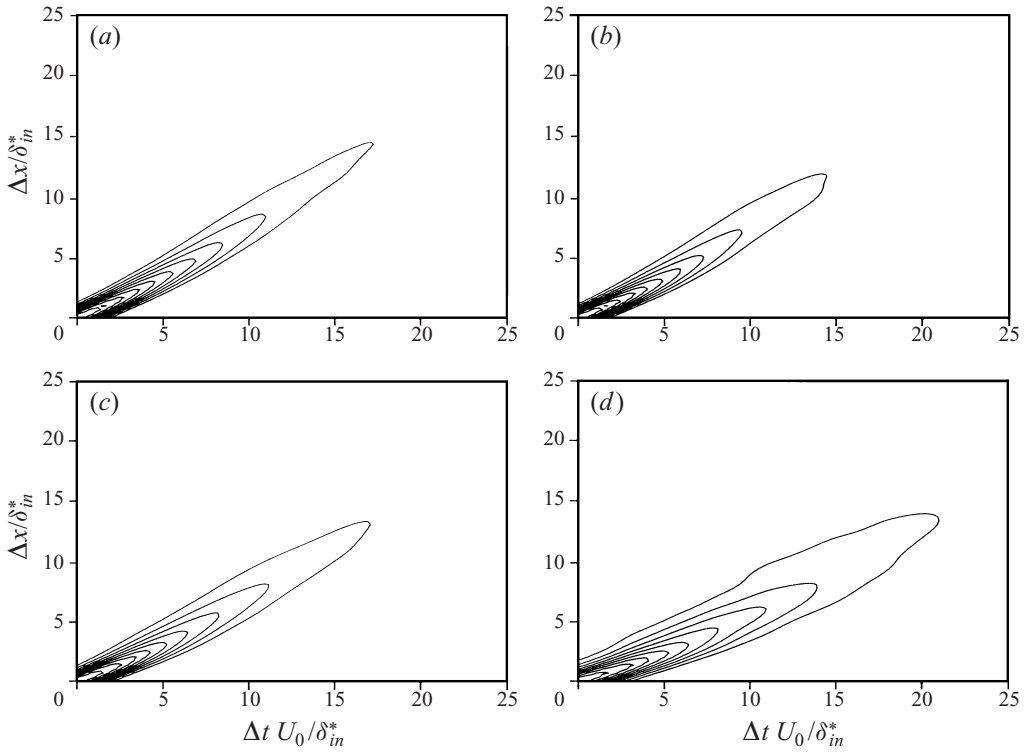

FIGURE 9. Contour plot of two-point correlation of wall-pressure fluctuations as a function of streamwise spatial and temporal separations. (*a*) $x = 0.5$; (*b*) $x = 0.6$; (*c*) $x = 0.7$; (*d*) $x = 0.85$. Contour levels are from 0.1 to 0.9 with increments of 0.1.

Space–time correlation functions are shown in figure 9. They also show the variation in size of large-scale structures as the streamwise pressure gradient varies. As shown in figure 9, through the FPG region, the large-scale pressure fluctuations become smaller in both time and streamwise directions and then grow in the APG region. The propagation speed of the eddies denoted by the slope $\mathrm{d}(\Delta x)/\mathrm{d}(\Delta t)$ is larger in the FPG region.

Convection velocity can be defined in a number of ways: a commonly used definition is the ratio $\Delta x/\Delta t$ which makes the space–time correlation of wall-pressure fluctuations maximum. Thus, the convection velocity defined in this way can be a function of either streamwise or temporal separations; these are presented in figures 10(*a*) and 10(*b*). It is apparent that more statistical samples are needed for smoother data. From figure 10, the large-scale structures have a convection velocity of about $0.89U_0$ or $0.83U_\infty$, where U_0 and U_∞ are the inlet and local free-stream velocities, respectively. The small-scale motions have a smaller velocity of $0.68U_0$ or $0.64U_\infty$ in the FPG region ($x = 0.5$ m). In the APG region, the large-scale motions have a convection velocity of $0.65U_0$ or $0.66U_\infty$ and the mean convection velocity of small-scale structures is as low as $0.48U_0$ or $0.49U_\infty$. In his experimental study of non-ZPG boundary layers, Schloemer (1967) showed, at one streamwise location, that the convection velocity (U_c/U_∞) as a function of longitudinal spatial separation varies from 0.7 at $\Delta x/\delta^* = 7.5$ (δ^* is the local displacement thickness) to 0.82 at large Δx in the FPG region. In the APG region, the convection velocity is decreased and it is about 0.5 at small separation. These results agree very well with the present

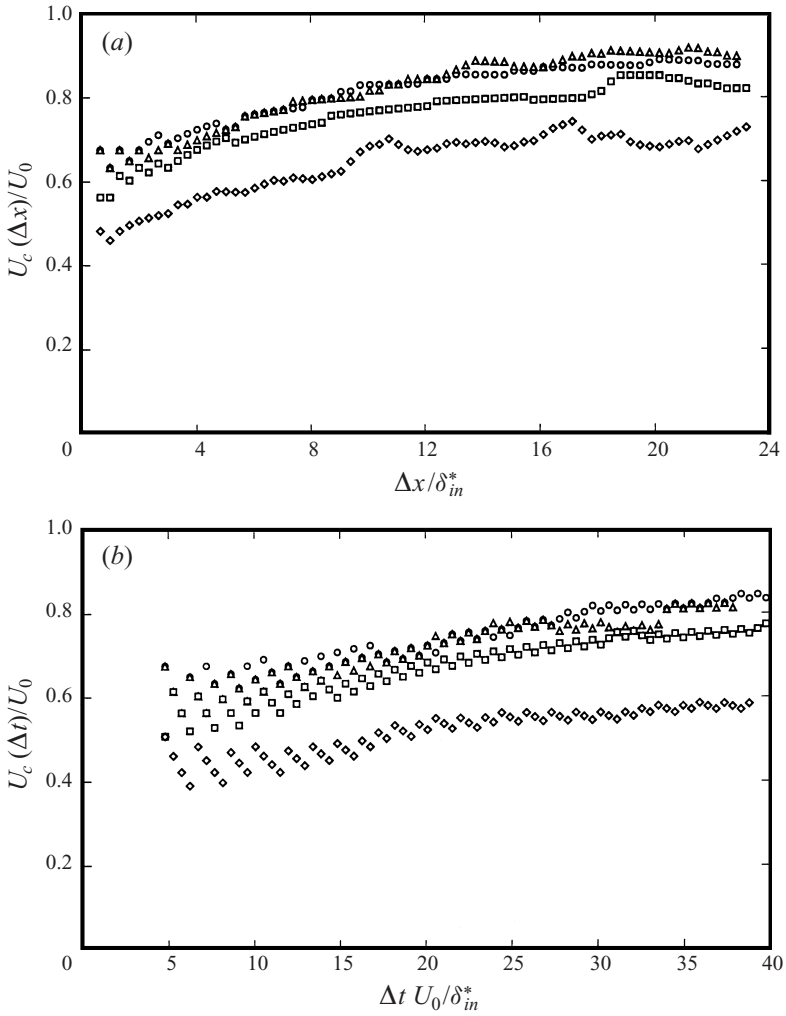

FIGURE 10. (*a*) Convection velocity $U_c(\Delta x)$ as a function of streamwise spatial separation, and (*b*) convection velocity $U_c(\Delta t)$ as a function of temporal separation. ○, $x = 0.5$; △, $x = 0.6$; □, $x = 0.7$; ◇, $x = 0.85$.

DNS results. In figure 10(*b*), the convection velocities are lower than those from figure 10(*a*) in both FPG and APG regions. Anomalies at small Δt are due to the coarse spatial resolution, Δx, compared to Δt.

4. Separated turbulent boundary layer

4.1. *Flow configuration*

The computational domain is shown in figure 2. The extent of the computational domain was chosen to be $350\delta^*_{in}$, $64\delta^*_{in}$ and $50\delta^*_{in}$ in the streamwise, wall-normal and spanwise directions, respectively. The upper boundary is located far away from the separation bubble so that turbulence intensities as well as vorticity are sufficiently small near the upper boundary.

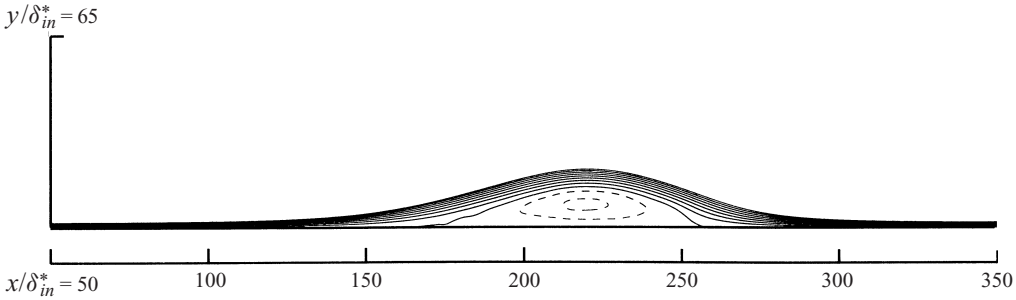

FIGURE 11. Mean streamlines for the separated turbulent boundary layer.

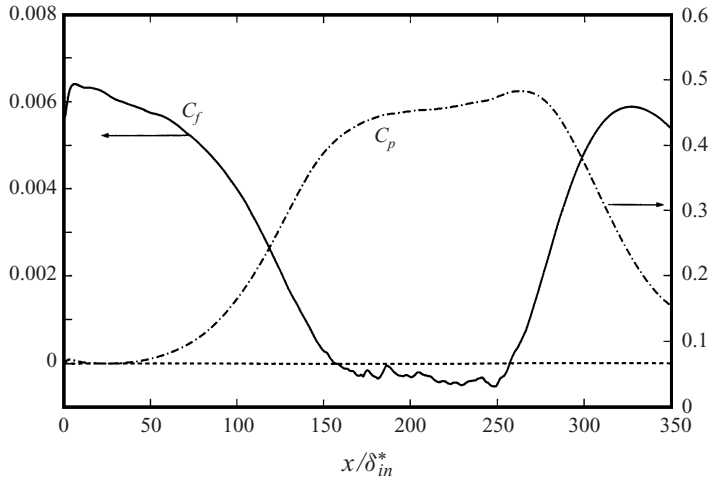

FIGURE 12. Skin friction and mean wall-pressure coefficient based on U_0.

The Reynolds number based on inlet momentum thickness and maximum mean streamwise velocity at inlet is 300. The mean streamlines are shown in figure 11. Due to the imposed boundary condition shown in figure 3(*b*), the flow firmly reattaches after the separation and develops under a FPG. The height of the separation bubble is about $22\theta_{in}$ (or $13\delta^*_{in}$) and the length of the bubble is about $170\theta_{in}$ (or $99.5\delta^*_{in}$). The intersections of the mean dividing streamline ($\psi = 0$) with the wall are at $x/\delta^*_{in} = 158$ and 257. The mean skin friction and the wall-pressure coefficients are shown in figure 12. To help turbulence develop and lose its memory of the initial transients due to inflow boundary conditions, the region of interest, the region with increasingly positive pressure gradient, is preceded by a ZPG region as implied by the $V_{top}(x)$ in figure 3(*b*). The overshoots in C_f and C_p in the immediate vicinity of the inlet of the computational domain are due to the transients associated with artificial inflow boundary conditions. After the initial transient, C_f recovers to the experimental data very quickly. The C_p curve shows that the flow develops under a ZPG (or very mild FPG) near the inlet and then undergoes an increasingly positive pressure gradient up to the detachment point ($x/\delta^*_{in} = 158$). After the reattachment ($x/\delta^*_{in} = 257$), the boundary layer re-develops and accelerates under a strong FPG. The flattened top of the pressure distribution is caused by the blockage due to the rapidly growing boundary layer. Detailed flow fields are described in Na & Moin (1998).

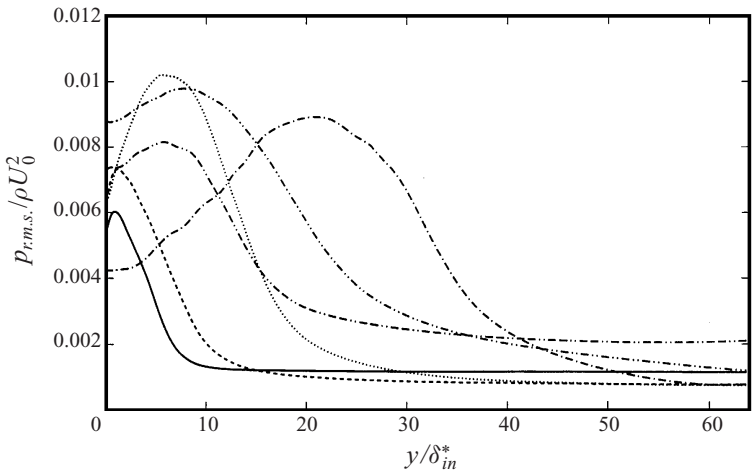

FIGURE 13. Profiles of root-mean-square pressure fluctuations. ——, $x/\delta^*_{in} = 80$; – – –, $x/\delta^*_{in} = 120$; · · · · ·, $x/\delta^*_{in} = 160$; — · —, $x/\delta^*_{in} = 220$; — · · —, $x/\delta^*_{in} = 270$; — — ··, $x/\delta^*_{in} = 320$.

The pressure on the wall was stored every 10 time steps (calculation time step Δt_{cal} was 0.03 δ^*_{in}/U_0). A total of 8000 samples were divided into $m = 7$ overlapping segments. Each segment contains 2000 samples and covers $T_N = 600\delta^*_{in}/U_0$. The resulting resolved frequency range is $0 \leqslant \omega \leqslant 10.5U_0/\delta^*_{in}$ with a frequency resolution of $\Delta\omega = 0.011U_0/\delta^*_{in}$. The statistical data were sampled at equal time intervals, $\Delta t_s = 0.3\delta^*_{in}/U_0$, or every 10 calculation time steps, and the total averaging time was $T_{ave} = 2400\delta^*_{in}/U_0$. This is equivalent to about five 'flow-through' times. The 'flow-through' time here is defined as the time required for a fluid particle outside the separation bubble to travel through the domain.

4.2. *Pressure fluctuation distribution*

Root-mean-square pressure fluctuations as a function of wall-normal distance are shown in figure 13. The wall-pressure fluctuations are reduced in the separated zone compared to those far upstream. However, they are enhanced in the reattachment region. The large r.m.s. values near reattachment are thought to be in part due to the wandering of the reattachment location and to the wide variation of turbulence structures impinging on the wall at reattachment. Away from the wall, the pressure fluctuations have significantly increased above the separation bubble compared to those far upstream (detached flow). This increase is thought to be due to the movement of vortical structures, which contribute to the generation of pressure fluctuation, away from the wall. Schewe (1983) and Kim (1989) estimated the location of the 'effective' source term for the pressure to be the distance from the wall where the mean velocity was equal to the convection velocity of the pressure fluctuations at the wall. The location of the effective source terms determined in this way is approximately the location where the dominant source term in the Poisson equation for pressure has its maximum. Most of the contributions to the source term come from the vortex structures near the wall (Kim 1989). In the separated flow, turbulent structures emanating upstream of separation move upwards into the shear layer in the detachment region and then turn around the bubble (Na & Moin 1998). Thus, the increase in pressure fluctuations away from the wall in the separated region is likely due to the movement of those vortical structures (or 'effective' sources for

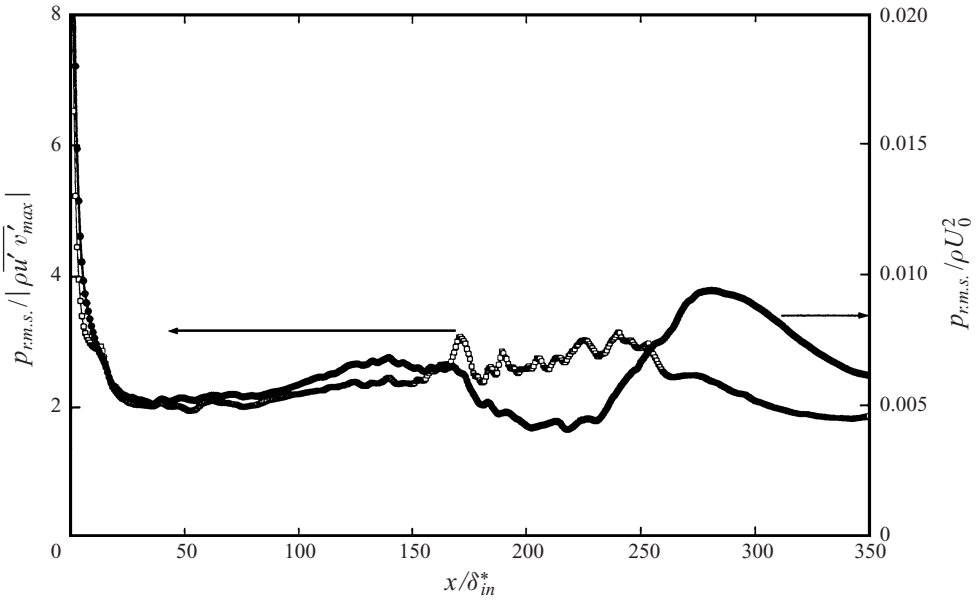

FIGURE 14. Streamwise distribution of wall-pressure fluctuations: •, normalized by reference dynamic pressure, ρU_0^2; ○, normalized by local maximum Reynolds shear stress, $-\rho\overline{u'v'}_{max}$.

the pressure) away from the wall. The behaviour of pressure fluctuations shown in figure 13 resembles that of turbulence intensities and Reynolds shear stress (Na & Moin 1996). Far upstream of the separation bubble, the location of maximum pressure fluctuations occurs very near the wall. Inside the separation bubble, however, the location of maximum fluctuations is far away from the wall and the pressure fluctuations are significantly enhanced away from the wall. In this region, Reynolds shear stresses and their gradients are large away from the wall and thus the largest pressure fluctuations are in the middle of the shear layer. After the reattachment, the flow starts to re-develop and the location of maximum r.m.s. pressure fluctuations moves towards the wall. There is a fair agreement in the positions of maximum pressure fluctuations and the maximum Reynolds shear stress.

Figure 14 shows the r.m.s. wall-pressure fluctuations normalized by the reference inlet dynamic pressure ρU_0^2 and the local maximum Reynolds shear stress $-\rho\overline{u'v'}_{max}$. There is less variation of wall-pressure fluctuations when normalized by $-\rho\overline{u'v'}_{max}$ than by the inlet dynamic pressure; the maximum turbulent shearing stress $-\rho\overline{u'v'}_{max}$ appears to be a better scale to normalize wall-pressure fluctuations in separated turbulent boundary layers (Simpson *et al.* 1987). This scaling will be further investigated for the power spectra of wall-pressure fluctuations in the next subsection. In Simpson *et al.*'s experiment, the wall-pressure fluctuations normalized by the reference dynamic pressure varied from 0.006 to 0.007 in the region of incipient detachment (note that the values at the reattachment are not available because the separation bubble was not closed in their experiment). If normalized by the local maximum Reynolds shear stress, the wall-pressure fluctuations varied from 4 to 5.5 in that region. Thus, the present results shown in figure 14 are well below their experimental data near the incipient detachment. This sizeable difference may be explained by the low Reynolds number effects shown by Choi & Moin (1990). They examined the available experimental and numerical data and showed that variation of the r.m.s. values of

wall-pressure fluctuations with Reynolds number is rather large ($p_{r.m.s.}$ at $Re_\theta = 13200$ is about 2.5 times that at $Re_\theta = 290$), indicating that pressure statistics are much slower to develop with Reynolds number than the r.m.s. velocity fluctuations and the mean velocity profile. Considering the sizeable difference in Reynolds numbers, the present results are within the variation shown by Choi & Moin.

4.3. *Power spectra of wall-pressure fluctuations*

Temporal signals of wall-pressure fluctuations at several streamwise locations are shown in figure 15. They show a wide-range of time scales. As one moves towards the detachment region, the frequency of the oscillations decreases significantly. Inside the separation bubble, the signal is dominated by low-frequency motions. A time sequence of contours of spanwise-averaged pressure fluctuations in the (x, y)-plane in Na & Moin (1998) shows significant differences in eddy length scales between the far upstream and the separated zone. The small-scale structures grow rapidly in the separated shear layer and the resulting two-dimensional roller-type structures convect downstream. In the shear layer near the detachment region, an alternating flow pattern (positive-and-then-negative contours of pressure fluctuations) develops. This is attributed to the passage of large two-dimensional vortical structures since the pressure is relatively low in the cores of vortices and it is relatively high between the cores. Thus, this long-time-scale behaviour in figure 15 is associated with the movement of large-scale structures generated in the shear layer due to an inflectional hydrodynamic instability as in mixing layers. The characteristic time of this shedding process varies from $tU_0/\delta^*_{in} = 100$ to 400 and the corresponding characteristic Strouhal number, $St = f\delta^*_{in}/U_0$, ranges between 0.0025 and 0.01. The presence of large-time-scale motion implies that a large statistical sample is required to get converged statistics inside the separation bubble. In view of the shedding process, total averaging time of the present work, $T_{ave} = 2250\delta^*_{in}/U_0$, is approximately equivalent to 8–9 passages of those structures assuming the characteristic time of the structures is about $(250\text{–}300)\delta^*_{in}/U_0$. Far downstream of the separation bubble, the signal regains high-intensity small-scale components superimposed on large-scale components.

Figures 16–18 show the wall-pressure spectra at several streamwise locations in two different non-dimensional coordinates. In figure 16 (*a*), $\phi(\omega)$ is normalized by the local free-stream dynamic pressure, q_∞, upstream of the incipient detachment. This scaling was used for the outer-layer similarity in § 3.3 and produces good collapse of the data. The frequency spectra normalized by the maximum Reynolds shear stress $-\rho\overline{u'v'}_{max}$ gives a similar result. Note that the q_∞ scaling gives better collapse than $-\rho\overline{u'v'}_{max}$ in the mild APG flow considered in § 3.3. It has been argued that the contribution of eddies in the logarithmic region to the wall pressure leads to a -1 slope in the power spectrum (Blake 1986). Since the Reynolds number considered in the present study is very low, the logarithmic layer is not well defined and the contribution to the wall pressure from this layer is negligible and so the $\phi(\omega) \sim \omega^{-1}$ region is not expected to be seen in figure 16 (*b*). At high frequencies, the spectra decay faster than ω^{-3} which is observed experimentally (Simpson *et al.* 1987) in the strong APG region. This might be partly due to the low Reynolds number effects and partly due to the effects of second-order finite-difference spatial discretization used in the present study. At low frequencies, the spectra level off and this behaviour can also be seen in the results of APG flow (§ 3.3) and some experimental data (Bradshaw 1967).

The frequency spectra inside the separation bubble are shown in figure 17. The q_∞ scaling which produces good collapse of data upstream of the separation bubble does not work very well in this region. The spectra normalized with maximum Reynolds

https://doi.org/10.1017/S0022112098003218 Published online by Cambridge University Press

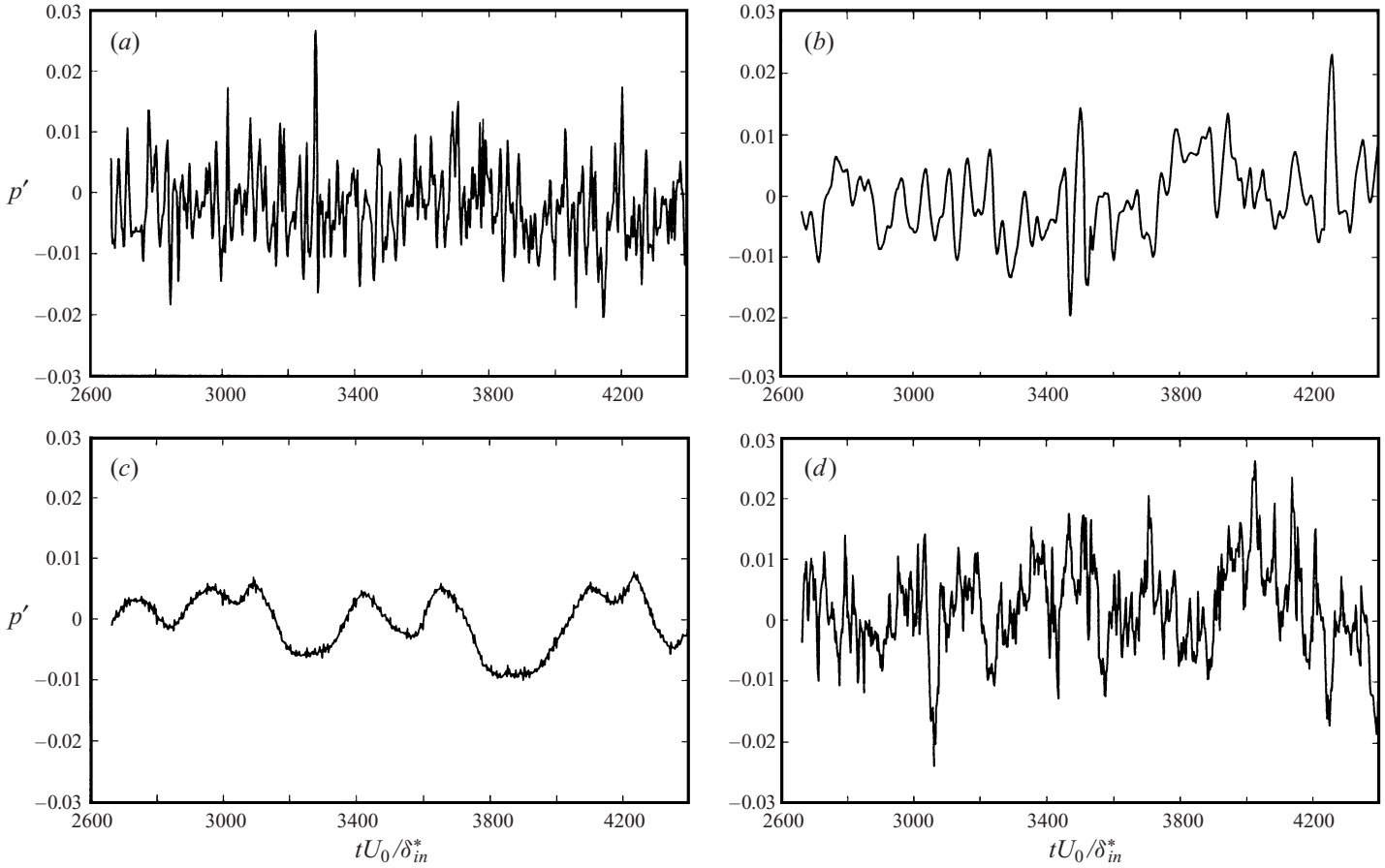

FIGURE 15. Time history of wall-pressure fluctuation $p'/\rho U_0^2$ at $z/\delta^*_{in} = 25$. (*a*) $x/\delta^*_{in} = 125$; (*b*) $x/\delta^*_{in} = 165$; (*c*) $x/\delta^*_{in} = 220$; (*d*) $x/\delta^*_{in} = 320$.

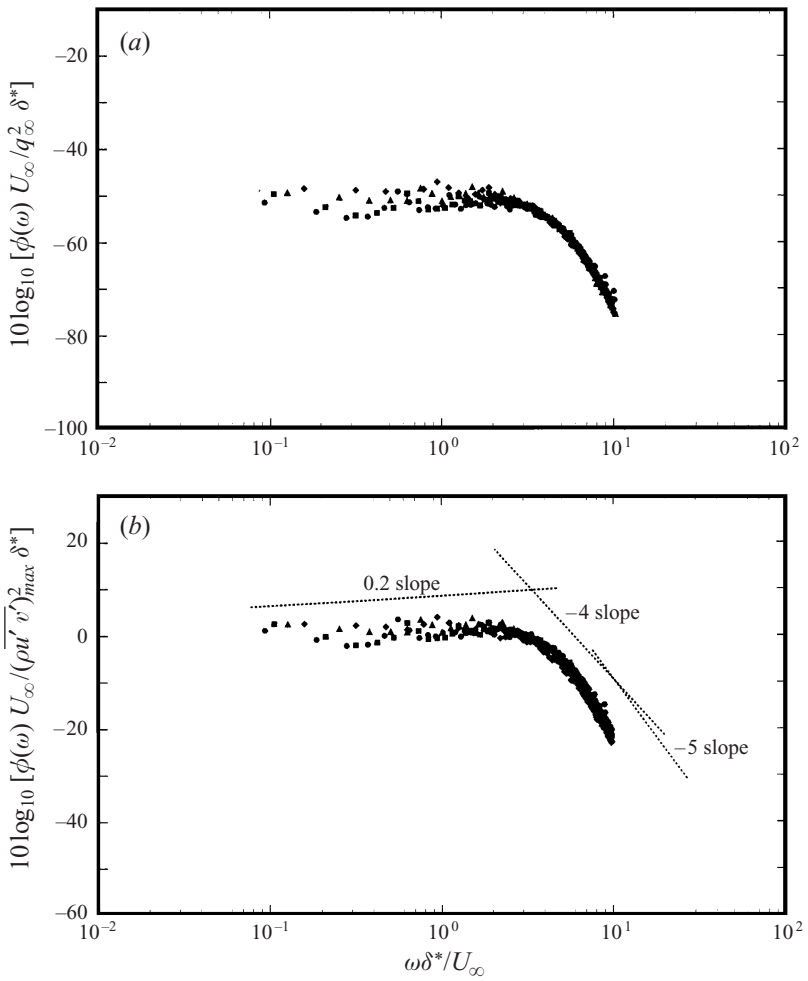

FIGURE 16. Frequency spectra of wall-pressure fluctuations. •, $x/\delta^*_{in} = 120$; □, $x/\delta^*_{in} = 130$; △, $x/\delta^*_{in} = 140$; ⋄, $x/\delta^*_{in} = 150$. Outer variable scaling with pressure scaled with (*a*) q^2_∞ and (*b*) $(\rho\overline{u'v'})^2_{max}$.

shear stress produce a good similarity, which indicates that the free-stream dynamic pressure has less direct influence on the wall-pressure spectra than the local maximum shearing stress inside the separation bubble. Simpson *et al.* (1987) used $-\rho\overline{u'v'}_{max}$ for a better collapse of their experimental data downstream of incipient detachment. Again, at high frequencies, spectra decay faster than ω^{-3}. In the low-frequency region, the spectra increase slightly. Simpson *et al.* observed a decrease in the spectra in the very low-frequency region (down to $\omega\delta^*/U_\infty \approx 0.0004$), but it is not possible to compare with their data since the present results were obtained only down to the frequency $\omega\delta^*/U_\infty \approx 0.4$.

The spectra downstream of reattachment are shown in figure 18. At high frequencies, the spectra show the ω^{-2} behaviour which is different from those upstream of detachment, indicating the wall-pressure field has not yet recovered from the separation.

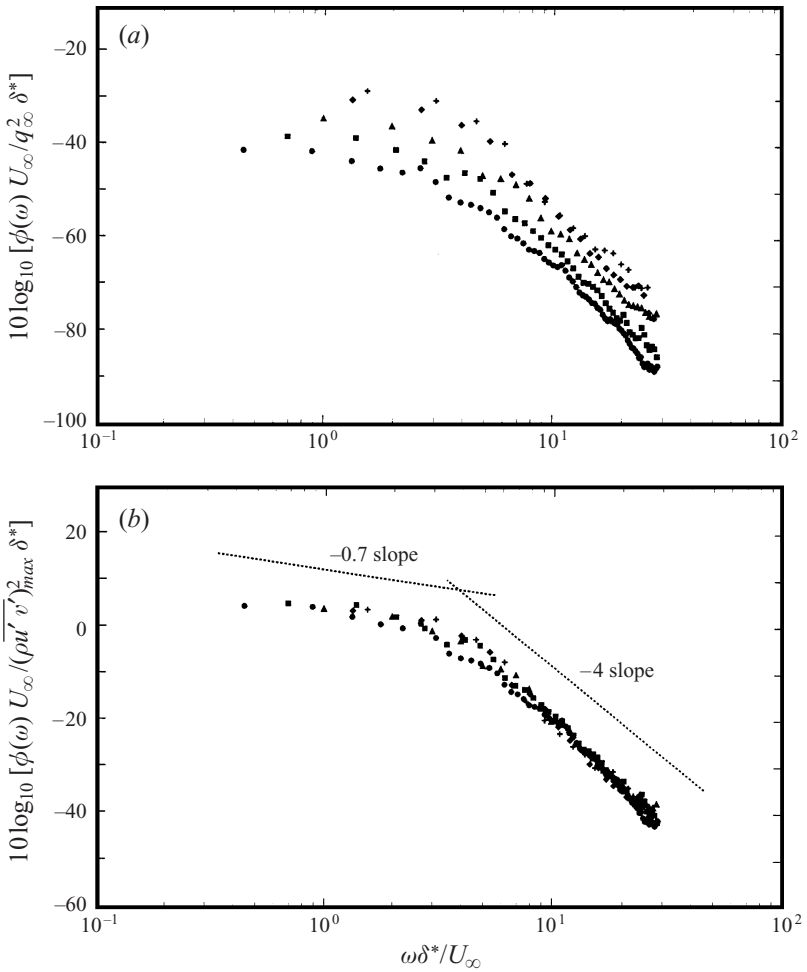

FIGURE 17. Frequency spectra of wall-pressure fluctuations. •, $x/\delta^*_{in} = 180$; □, $x/\delta^*_{in} = 190$; △, $x/\delta^*_{in} = 200$; ⋄, $x/\delta^*_{in} = 210$; +, $x/\delta^*_{in} = 220$. Outer variable scaling with pressure scaled with (*a*) q^2_∞ and (*b*) $(\rho\overline{u'v'})^2_{max}$.

4.4. *Two-point correlation*

In figure 19, contour plots of two-point correlation of wall-pressure fluctuations as a function of streamwise and spanwise spatial separations are shown. Far upstream of separation, the contour shapes are similar to those of APG flow (figure 8). Inside the separation bubble ($x/\delta^*_{in} = 220$), the contours are highly elongated in the spanwise direction which implies the presence of large two-dimensional structure in this region as explained in §4.3. The reattachment region ($x/\delta^*_{in} = 270$) is also dominated by the quasi-two-dimensional structures. Downstream of the bubble ($x/\delta^*_{in} = 320$) where the flow field redevelops under strong FPG, the flow begins to recover and the shapes of contours slowly revert back to those of attached boundary layers. However, in the recovery region, the effect of large quasi-two-dimensional structures is still pronounced. At this location, the small-scale fluctuations make the oval contribution to the contours at small separations (which are more elongated in the streamwise direction than in the spanwise direction). Thus, it appears that smaller eddies (which

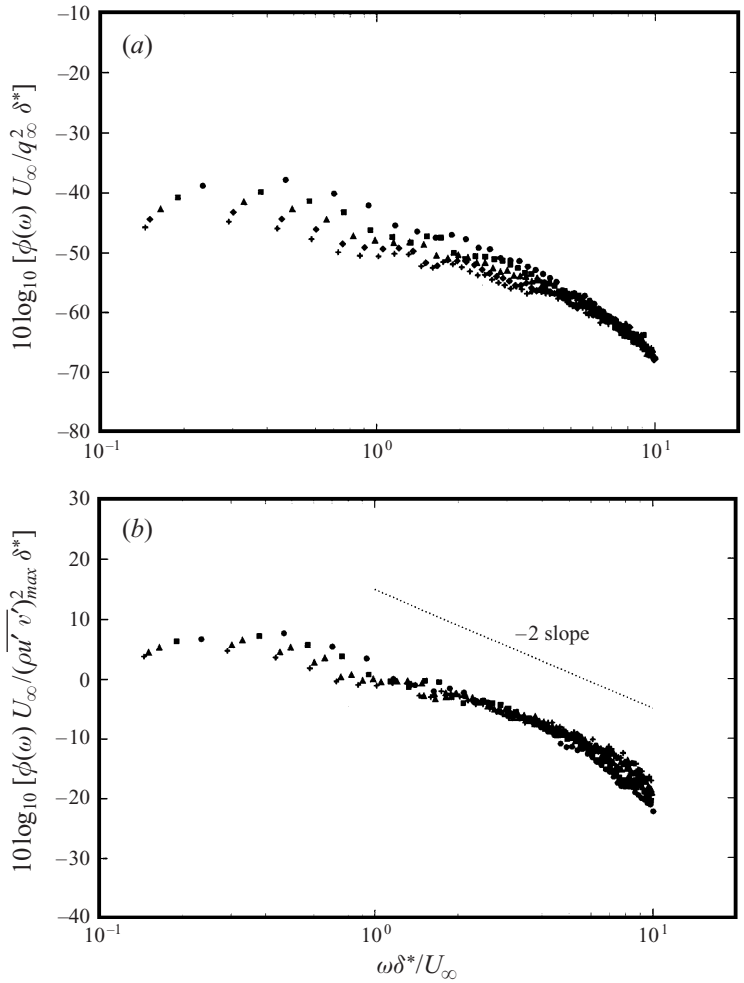

FIGURE 18. Frequency spectrum of wall-pressure fluctuations. •, $x/\delta^*_{in} = 280$; □, $x/\delta^*_{in} = 290$; △, $x/\delta^*_{in} = 300$; ◇, $x/\delta^*_{in} = 310$; +, $x/\delta^*_{in} = 320$. Outer variable scaling with pressure scaled with (*a*) q^2_∞ and (*b*) $(\rho\overline{u'v'})^2_{max}$.

have a smaller time scale) react faster to the strong FPG than the larger eddies and, as a result, the shapes of the contours at small separations evolve relatively faster. For comparison, contours of constant two-point correlations of the streamwise velocity fluctuations near the wall are shown in figure 20. Two-point correlations upstream of detachment ($x/\delta^*_{in} = 80, 120$) illustrate the presence of the streaky structures elongated in the streamwise direction. Since the large-scale structures contributing to wall-pressure fluctuations are more elongated in the spanwise direction than those of velocity fluctuations in the vicinity of the wall, it appears that the sources for large-scale pressure fluctuations are in the outer layers. The streamwise elongation disappears slowly and contours become circular as the flow approaches the incipient detachment ($x/\delta^*_{in} = 160$) due to the rapid deceleration of the fluid in this region. Note that the streaky structures disappear in this region. Inside the separation bubble ($x/\delta^*_{in} = 220$) and in the reattachment region ($x/\delta^*_{in} = 270$), the contours are more elongated in the spanwise direction similar to those of pressure fluctuations due to the presence of large two-dimensional structures. Far downstream of the separation

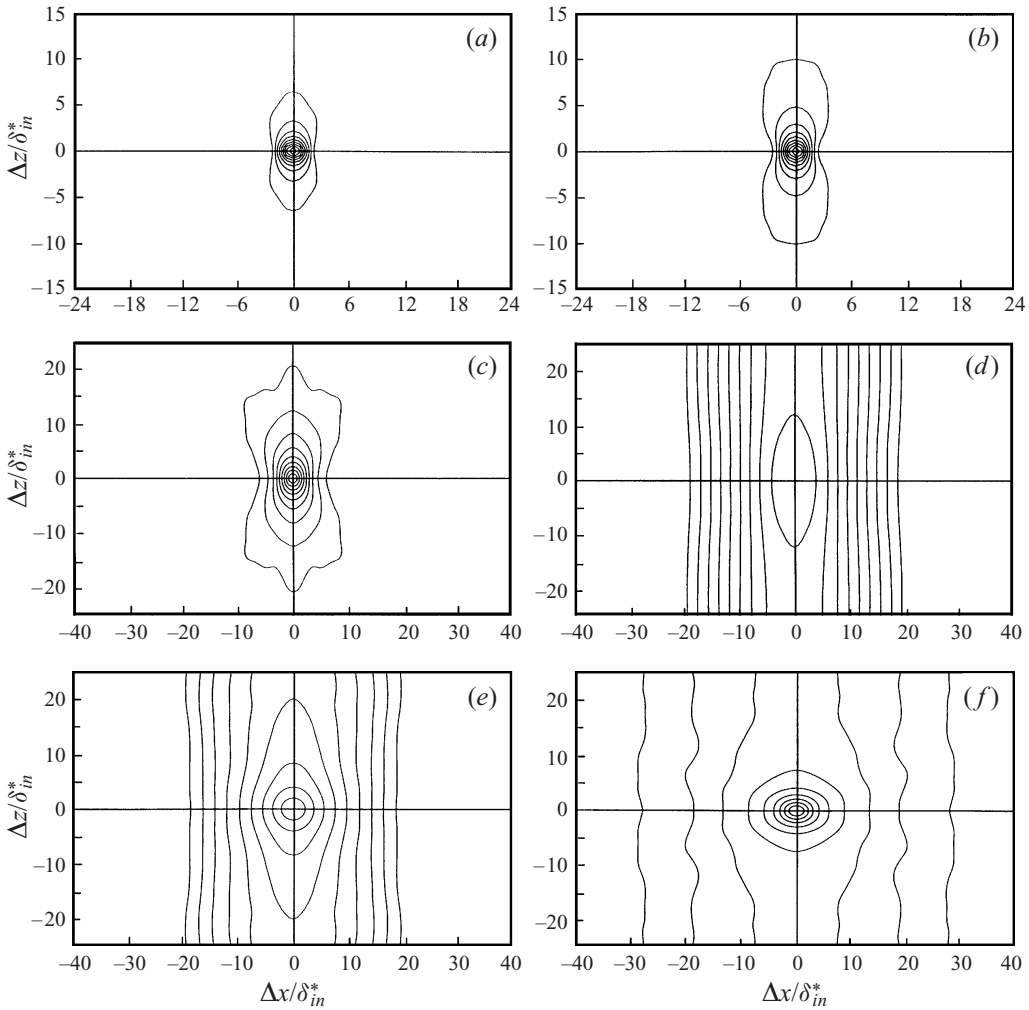

FIGURE 19. Contour plot of two-point correlation of wall-pressure fluctuations as a function of streamwise and spanwise separations. (*a*) $x/\delta^*_{in} = 80$; (*b*) $x/\delta^*_{in} = 120$; (*c*) $x/\delta^*_{in} = 160$; (*d*) $x/\delta^*_{in} = 220$; (*e*) $x/\delta^*_{in} = 270$; (*f*) $x/\delta^*_{in} = 320$. Contour levels are from 0.1 to 0.9 with increments of 0.1.

bubble ($x/\delta^*_{in} = 320$), the streamwise elongation becomes pronounced again as the flow recovers, whereas contours of pressure fluctuations remain elongated in the spanwise direction.

4.5. *Space–time correlation*

Contours of space–time correlations (figure 21) show that the convection velocities of wall-pressure fluctuations decrease as the pressure gradient increases and they are significantly reduced inside the separation bubble. The contour plots clearly show that the convected pressure field slowly loses its coherence as convection proceeds and the correlation decays more slowly in the separated region. The small bump in figure 21 (*e*) at $\Delta t U_0/\delta^*_{in} = 100$ is associated with the quasi-periodic inflow signal discussed in § 2.

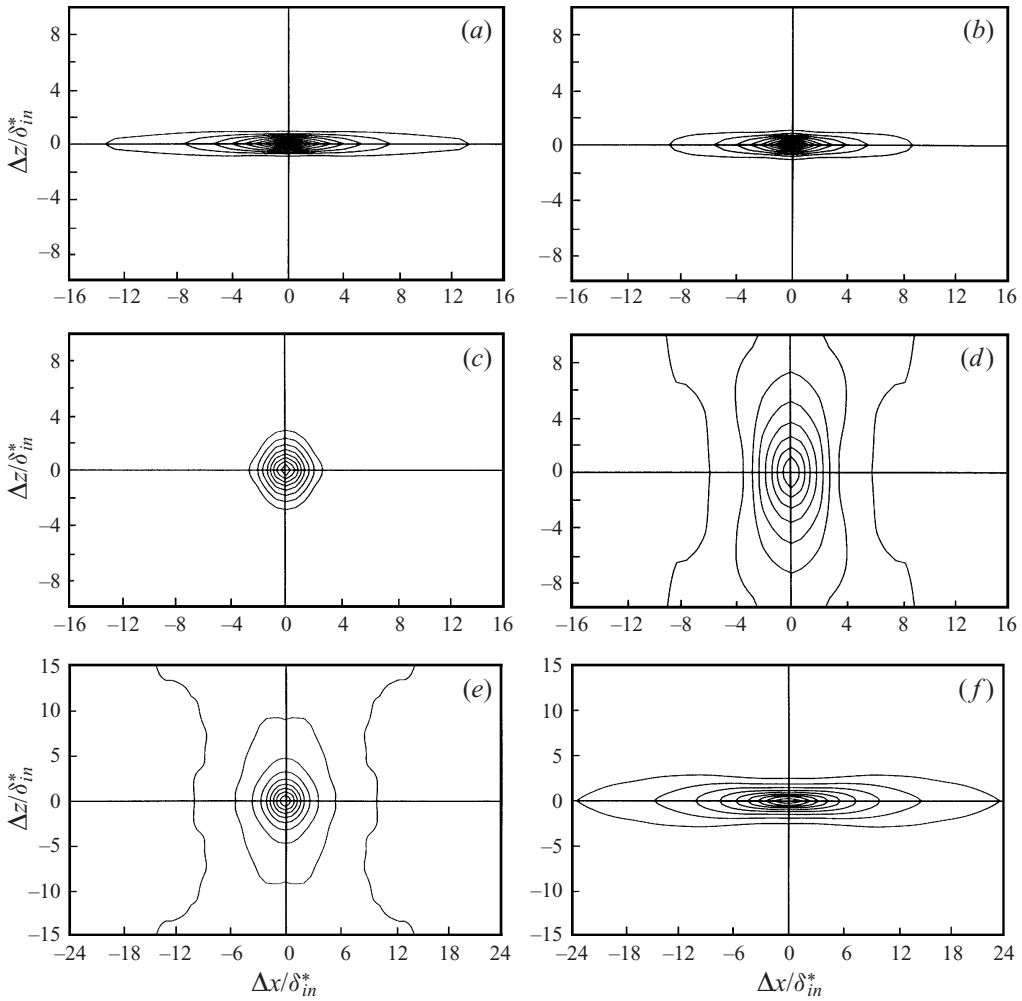

FIGURE 20. Contour plot of two-point correlation of streamwise velocity fluctuations as a function of streamwise and spanwise separations at $y/\delta^*_{in} = 0.0042$. (*a*) $x/\delta^*_{in} = 80$; (*b*) $x/\delta^*_{in} = 120$; (*c*) $x/\delta^*_{in} = 160$; (*d*) $x/\delta^*_{in} = 220$; (*e*) $x/\delta^*_{in} = 270$; (*f*) $x/\delta^*_{in} = 320$. Contour levels are from 0.1 to 0.9 with increments of 0.1.

The pressure would appear coherent only for short times to an observer at a fixed point in space, but it would lose its coherence much slower to an observer moving with the field so as to be at the position of maximum longitudinal space–time correlation. The variation of Δt_c, the time delay for which the $\Delta x =$ constant curve of the space–time correlation of wall-pressure is a maximum, defines a moving reference frame relative to which the decay rate of the correlation is a minimum. The velocity of this reference frame $U_c = \Delta x/\Delta t_c$ for a given Δx, as defined by Bull (1967), provides another definition of convection velocity and is displayed in figure 22 (*a*). In this figure, the convection velocities decrease significantly from $x/\delta^*_{in} = 80$ to $x/\delta^*_{in} = 220$, and then increase downstream. At $x/\delta^*_{in} = 220$, the convection velocity takes the value of $0.33U_0$ at large Δx. Figure 22 (*b*) displays the convection velocities shown in figure 22 (*a*) normalized by the local free-stream velocity. It shows that normalization

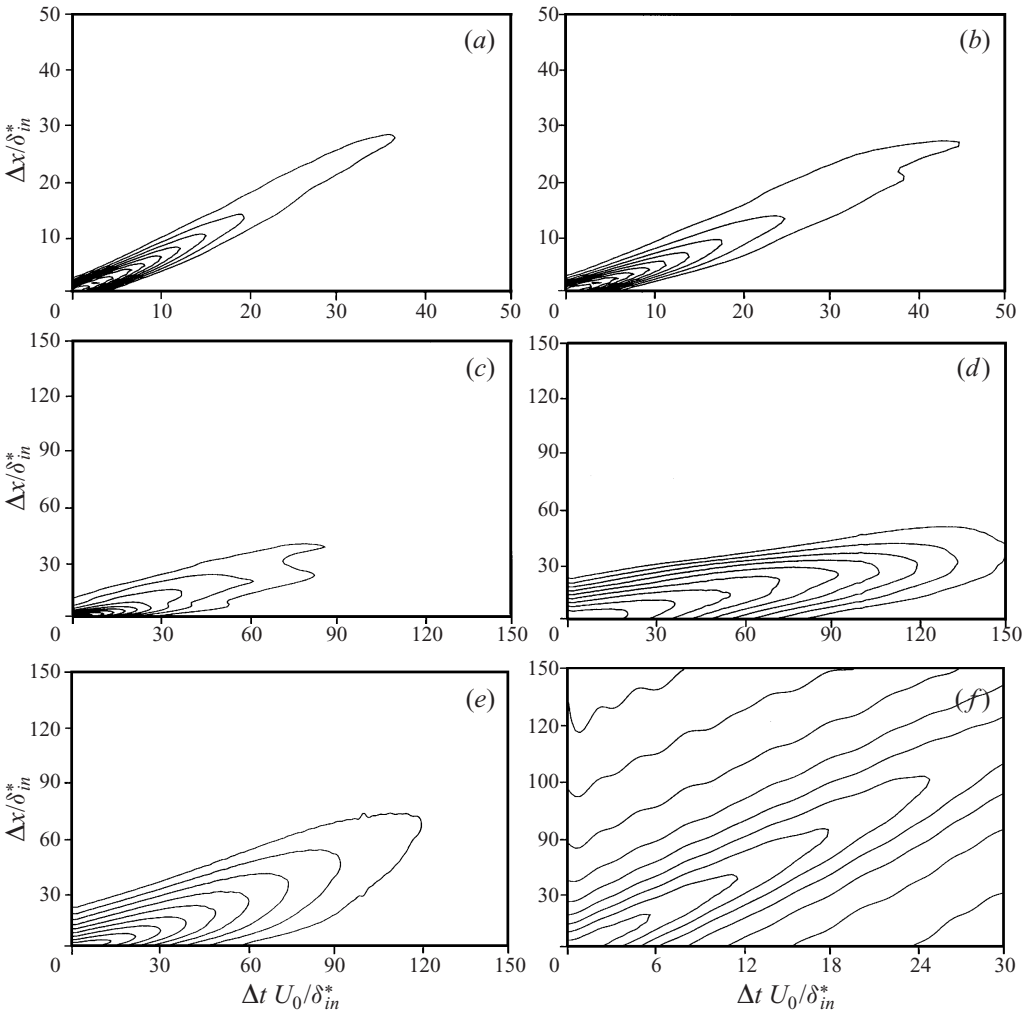

FIGURE 21. Contour plot of two-point correlation of wall-pressure fluctuations as a function of streamwise spatial and temporal separations. (*a*) $x/\delta^*_{in} = 80$; (*b*) $x/\delta^*_{in} = 120$; (*c*) $x/\delta^*_{in} = 160$; (*d*) $x/\delta^*_{in} = 220$; (*e*) $x/\delta^*_{in} = 270$; (*f*) $x/\delta^*_{in} = 320$. Contour levels are from 0.1 to 0.9 with increments of 0.1.

with the local free-stream velocity results in less variation of the convection velocity. Inside the separation bubble ($x/\delta^*_{in} = 220$), the convection velocity takes an average value of about $0.55U_\infty$ and the convection velocities in the recovery region are higher than those in the upstream region.

5. Conclusion

Space–time characteristics of wall-pressure fluctuations in two spatially developing turbulent boundary layers have been investigated. In the first case, the adverse pressure gradient is mild, and the boundary layer remains attached. In the second case, the boundary layer undergoes separation and reattachment with a closed separation bubble.

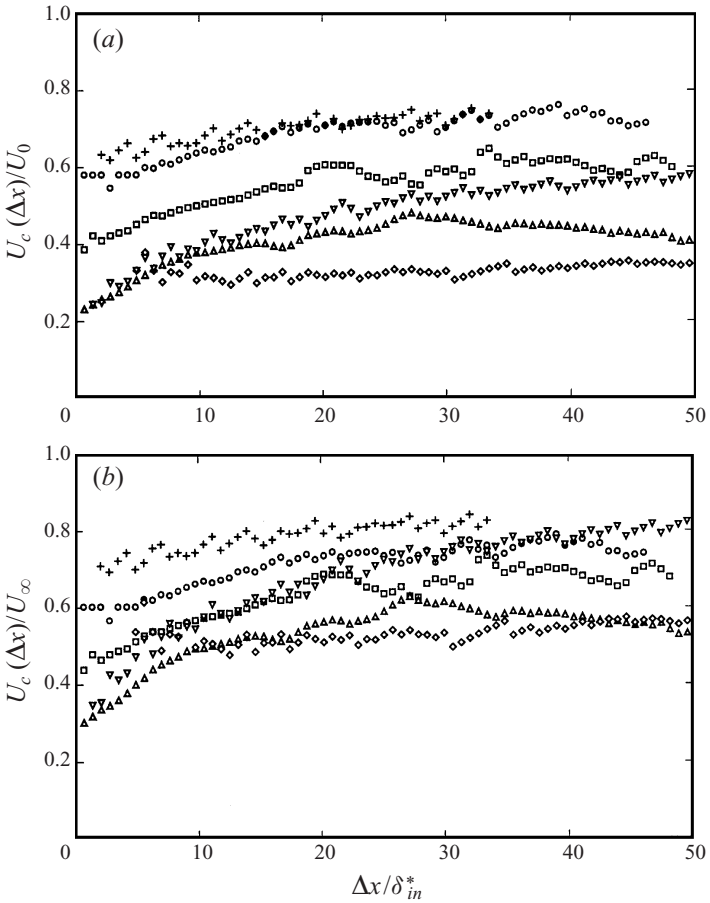

FIGURE 22. (*a*) Convection velocity $U_c(\Delta x)$ as a function of streamwise spatial separation, and (*b*) convection velocity $U_c(\Delta x)$ as a function of streamwise spatial separation normalized by local free-stream velocity U_∞. ○, $x/\delta^*_{in} = 80$; □, $x/\delta^*_{in} = 120$; △, $x/\delta^*_{in} = 160$; ◇, $x/\delta^*_{in} = 220$; ▽, $x/\delta^*_{in} = 270$.

In the attached boundary layer with non-zero pressure gradient, frequency spectra of wall-pressure fluctuations normalized with the outer variables show very good correlation at low frequencies and the power increases in the high-frequency range as the streamwise pressure gradient increases. Contours of two-point spatial correlation of pressure fluctuations are more elongated in the spanwise direction in the adverse pressure gradient region. Convection velocity of the wall-pressure field is higher in the favourable pressure gradient region and the pressure field loses its coherence more slowly in the adverse pressure gradient region.

In the separated turbulent boundary layer, before the incipient detachment point, power spectra normalized by local free-stream dynamic pressure and local maximum Reynolds shear stress show good collapse. Inside the separation bubble, however, only the spectra normalized by local maximum Reynolds shear stress correlate well. This indicates that the free-stream dynamic pressure has less direct influence on the wall-pressure spectra than the local maximum shearing stress inside the separation bubble. Downstream of the separation bubble, the spectra normalized by the local maximum Reynolds shear stress show better collapse than those normalized by the local dynamic

pressure. Contour plots of two-point correlation of wall-pressure fluctuations in the (x, z)-plane are highly elongated in the spanwise direction inside the separation bubble implying the presence of large two-dimensional roller-type structures. The convection velocity determined from the space–time correlation of pressure fluctuations is as low as $0.33U_0$ in the separated zone and increases downstream of reattachment.

This work was supported by the Office of Naval Research. The authors gratefully acknowledge Dr Meng Wang for his helpful comments and suggestions on a draft of this paper.

REFERENCES

Blake, W. K. 1970 Turbulent boundary-layer wall-pressure fluctuations. *J. Fluid Mech.* **44**, 637–660.

Blake, W. K. 1986 *Mechanics of Flow-Induced Sound and Vibration I, II*. Academic.

Bradshaw, P. 1967 Irrotational fluctuations near a turbulent boundary layer. *J. Fluid Mech.* **27**, 209–230.

Bull, M. K. 1967 Wall-pressure fluctuations associated with subsonic turbulent boundary layer flow. *J. Fluid Mech.* **28**, 719–754.

Choi, H. & Moin, P. 1990 On the space–time characteristics of wall-pressure fluctuations. *Phys. Fluids* A **2**, 1450–1460.

Eckelmann, H. 1989 A review of knowledge on pressure fluctuations. In *Near-Wall Turbulence* (ed. S. J. Kline & N. H. Afgan), pp. 328–347. Hemisphere.

Farabee, T. M. & Casarella, M. J. 1991 Spectral features of wall-pressure fluctuations beneath turbulent boundary layer. *Phys. Fluids* A **3**, 2410–2420.

Handler, R. A., Hansen, R. J., Sakell, S. A., Orszag, S. A. & Bullister, E. 1984 Calculation of the wall-pressure field in a turbulent channel flow. *Phys. Fluids* **27**, 579–582.

Inman, P. N. & Bradshaw, P. 1981 Mixing length in low Reynolds number turbulent boundary layers. *AIAA J.* **19**, 653–655.

Kim, J. 1989 On the structure of pressure fluctuations in simulated turbulent channel flow. *J. Fluid Mech.* **205**, 421–451.

Kim, J., Moin, P. & Moser, R. 1987 Turbulence statistics in fully developed channel flow at low Reynolds number. *J. Fluid Mech.* **177**, 133–166.

Kiya, A., Sasaki, K. & Arie, M. 1982 Discrete-vortex simulation of a turbulent separation bubble. *J. Fluid Mech.* **120**, 219–244.

Le, H. & Moin, P. 1991 An improvement of fractional step methods for the incompressible Navier–Stokes equations. *J. Comput. Phys.* **92**, 369–379.

Mabey, D. G. 1972 Analysis and correlation of data on pressure fluctuations in separated flow. *J. Aircraft* **9**, 642–645.

Mabey, D. G. 1982 Comment on "A review of research on subsonic turbulent flow attachment". *AIAA J.* **20**, 1632.

Mahesh, K., Moin, P. & Lele, S. K. 1996 The interaction of a shock wave with a turbulent shear flow. *Rep.* TF-69. Thermoscience Division, Dept. of Mech. Eng., Stanford University.

Na, Y. & Moin, P. 1996 Direct numerical simulation of turbulent boundary layer with adverse pressure gradient and separation. *Rep.* TF-68. Thermoscience Division, Dept. of Mech. Eng., Stanford University.

Na, Y. & Moin, P. 1998 Direct numerical simulation of separated turbulent boundary layer. *J. Fluid Mech.* **370**, 175–201.

Neves, J. & Moin, P. 1994 Effects of convex transverse curvature on wall-bounded turbulence. Part 2. The pressure fluctuations. *J. Fluid Mech.* **272**, 383–406.

Pauley, L. L., Moin, P. & Reynolds, W. C. 1990 The structure of two-dimensional separation. *J. Fluid Mech.* **220**, 397–411.

Schewe, G. 1983 On the structure and resolution of wall-pressure fluctuations associated with turbulent boundary-layer flow. *J. Fluid Mech.* **134**, 311–328.

Schloemer, H. H. 1967 Effects of pressure gradient on turbulent boundary layer wall-pressure fluctuations. *J. Acoust. Soc. Am.* **42**, 93–113.

Simpson, R. L., Ghodbane, M. & McGrath, B. E. 1987 Surface pressure fluctuations in a separating turbulent boundary layer. *J. Fluid Mech.* **177**, 167–186.

Spalart, P. R. 1988 Direct numerical simulation of a turbulent boundary layer up to $Re_\theta = 1410$. *J. Fluid Mech.* **187**, 61–98.

Spalart, P. R. & Watmuff, J. H. 1993 Experimental and numerical study of a turbulent boundary layer with pressure gradient. *J. Fluid Mech.* **249**, 337–371.

Watmuff, J. H. 1989 An experimental investigation of a low Reynolds number turbulent boundary layer subject to an adverse pressure gradient. *Ann. Res. Briefs, Center for Turbulence Research, NASA Ames Research Center/Stanford University*, pp. 37–49.

Willmarth, W. W. 1956 Wall pressure fluctuations in a turbulent boundary layer. *J. Acoust. Soc. Am.* **28**, 1048–1053.

Willmarth, W. W. 1975 Pressure fluctuations beneath turbulent boundary layers. *Ann. Rev. Fluid Mech.* **7**, 13–38.